Variable velocity range imaging of the choroid with dual-beam optical coherence angiography

Franck Jaillon, Shuichi Makita, and Yoshiaki Yasuno*

Computational Optics Group, University of Tsukuba, 1-1-1 Tennodai, Tsukuba, Ibaraki 305-8573, Japan
yasuno@optlab2.bk.tsukuba.ac.jp

Abstract: In this study, we present dual-beam Doppler optical coherence angiography with variable beam separation. Altering beam distance, independently of the scanning protocol, provides a flexible way to select the velocity range of detectable blood flow. This system utilized a one-micrometer wavelength light source to visualize deep into the posterior eye, i.e., the choroid. Two-dimensional choroidal vasculature maps of a human subject acquired with different beam separations, and hence with several velocity ranges, are presented. Combining these maps yields a semi-quantitative visualization of axial velocity of the choroidal circulation. The proposed technique may be useful for identifying choroidal abnormalities that occur in pathological conditions of the eye.

OCIS codes: (170.4500) Optical coherence tomography; (170.4470) Ophthalmology; (170.3880) Medical and biological imaging.

References and links

1. B. Feigl, "Age-related maculopathy - linking aetiology and pathophysiological changes to the ischaemia hypothesis," Prog. Retin. Eye Res. **28**(1), 63–86 (2009).
2. T. A. Ciulla, A. Harris, H. S. Chung, R. P. Danis, L. Kagemann, L. McNulty, L. M. Pratt, and B. J. Martin, "Color Doppler imaging discloses reduced ocular blood flow velocities in nonexudative age-related macular degeneration," Am. J. Ophthalmol. **128**(1), 75–80 (1999).
3. B. Pemp and L. Schmetterer, "Ocular blood flow in diabetes and age-related macular degeneration," Can. J. Ophthalmol. **43**(3), 295–301 (2008).
4. E. Friedman, "A hemodynamic model of the pathogenesis of age-related macular degeneration," Am. J. Ophthalmol. **124**(5), 677–682 (1997).
5. J. E. Grunwald, T. I. Metelitsina, J. C. Dupont, G. S. Ying, and M. G. Maguire, "Reduced foveolar choroidal blood flow in eyes with increasing AMD severity," Invest. Ophthalmol. Vis. Sci. **46**(3), 1033–1038 (2005).
6. D. Huang, E. A. Swanson, C. P. Lin, J. S. Schuman, W. G. Stinson, W. Chang, M. R. Hee, T. Flotte, K. Gregory, C. A. Puliafito, and J. G. Fujimoto, "Optical coherence tomography," Science **254**(5035), 1178–1181 (1991).
7. S. Radhakrishnan, A. M. Rollins, J. E. Roth, S. Yazdanfar, V. Westphal, D. S. Bardenstein, and J. A. Izatt, "Real-time optical coherence tomography of the anterior segment at 1310 nm," Arch. Ophthalmol. **119**(8), 1179–1185 (2001).
8. Y. Yasuno, V. D. Madjarova, S. Makita, M. Akiba, A. Morosawa, C. Chong, T. Sakai, K.-P. Chan, M. Itoh, and T. Yatagai, "Three-dimensional and high-speed swept-source optical coherence tomography for in vivo investigation of human anterior eye segments," Opt. Express **13**(26), 10652–10664 (2005).
9. E. A. T. Say, S. U. Shah, S. Ferenczy, and C. L. Shields, "Optical coherence tomography of retinal and choroidal tumors," J. Ophthalmol. **2011**, 385058 (2011).
10. W. Drexler and J. G. Fujimoto, "State-of-the-art retinal optical coherence tomography," Prog. Retin. Eye Res. **27**(1), 45–88 (2008).
11. R. A. Costa, M. Skaf, L. A. Melo, Jr., D. Calucci, J. A. Cardillo, J. C. Castro, D. Huang, and M. Wojtkowski, "Retinal assessment using optical coherence tomography," Prog. Retin. Eye Res. **25**(3), 325–353 (2006).
12. L. M. Sakata, J. Deleon-Ortega, V. Sakata, and C. A. Girkin, "Optical coherence tomography of the retina and optic nerve - a review," Clin. Experiment. Ophthalmol. **37**(1), 90–99 (2009).
13. E. C. W. Lee, J. F. de Boer, M. Mujat, H. Lim, and S. H. Yun, "In vivo optical frequency domain imaging of human retina and choroid," Opt. Express **14**(10), 4403–4411 (2006).
14. B. Povãzay, K. Bizheva, B. Hermann, A. Unterhuber, H. Sattmann, A. Fercher, W. Drexler, C. Schubert, P. Ahnelt, M. Mei, R. Holzwarth, W. Wadsworth, J. Knight, and P. S. J. Russell, "Enhanced visualization of

#157238 - $15.00 USD Received 28 Oct 2011; revised 9 Dec 2011; accepted 11 Dec 2011; published 21 Dec 2011

choroidal vessels using ultrahigh resolution ophthalmic OCT at 1050 nm," Opt. Express **11**(17), 1980–1986 (2003).
15. Y. Yasuno, Y. Hong, S. Makita, M. Yamanari, M. Akiba, M. Miura, and T. Yatagai, "In vivo high-contrast imaging of deep posterior eye by 1-µm swept source optical coherence tomography and scattering optical coherence angiography," Opt. Express **15**(10), 6121–6139 (2007).
16. D. M. de Bruin, D. L. Burnes, J. Loewenstein, Y. Chen, S. Chang, T. C. Chen, D. D. Esmaili, and J. F. de Boer, "In vivo three-dimensional imaging of neovascular age-related macular degeneration using optical frequency domain imaging at 1050 nm," Invest. Ophthalmol. Vis. Sci. **49**(10), 4545–4552 (2008).
17. V. J. Srinivasan, D. C. Adler, Y. Chen, I. Gorczynska, R. Huber, J. S. Duker, J. S. Schuman, and J. G. Fujimoto, "Ultrahigh-speed optical coherence tomography for three-dimensional and en face imaging of the retina and optic nerve head," Invest. Ophthalmol. Vis. Sci. **49**(11), 5103–5110 (2008).
18. Y. Zhao, Z. Chen, C. Saxer, S. Xiang, J. F. de Boer, and J. S. Nelson, "Phase-resolved optical coherence tomography and optical Doppler tomography for imaging blood flow in human skin with fast scanning speed and high velocity sensitivity," Opt. Lett. **25**(2), 114–116 (2000).
19. R. Leitgeb, L. Schmetterer, W. Drexler, A. Fercher, R. Zawadzki, and T. Bajraszewski, "Real-time assessment of retinal blood flow with ultrafast acquisition by color Doppler Fourier domain optical coherence tomography," Opt. Express **11**(23), 3116–3121 (2003).
20. J. A. Izatt, M. D. Kulkarni, S. Yazdanfar, J. K. Barton, and A. J. Welch, "In vivo bidirectional color Doppler flow imaging of picoliter blood volumes using optical coherence tomography," Opt. Lett. **22**(18), 1439–1441 (1997).
21. R. M. Werkmeister, N. Dragostinoff, M. Pircher, E. Götzinger, C. K. Hitzenberger, R. A. Leitgeb, and L. Schmetterer, "Bidirectional Doppler Fourier-domain optical coherence tomography for measurement of absolute flow velocities in human retinal vessels," Opt. Lett. **33**(24), 2967–2969 (2008).
22. L. Yu and Z. Chen, "Doppler variance imaging for three-dimensional retina and choroid angiography," J. Biomed. Opt. **15**(1), 016029 (2010).
23. S. Makita, Y. Hong, M. Yamanari, T. Yatagai, and Y. Yasuno, "Optical coherence angiography," Opt. Express **14**(17), 7821–7840 (2006).
24. Y. Hong, S. Makita, M. Yamanari, M. Miura, S. Kim, T. Yatagai, and Y. Yasuno, "Three-dimensional visualization of choroidal vessels by using standard and ultra-high resolution scattering optical coherence angiography," Opt. Express **15**(12), 7538–7550 (2007).
25. A. H. Bachmann, M. L. Villiger, C. Blatter, T. Lasser, and R. A. Leitgeb, "Resonant Doppler flow imaging and optical vivisection of retinal blood vessels," Opt. Express **15**(2), 408–422 (2007).
26. Y. K. Tao, K. M. Kennedy, and J. A. Izatt, "Velocity-resolved 3D retinal microvessel imaging using single-pass flow imaging spectral domain optical coherence tomography," Opt. Express **17**(5), 4177–4188 (2009).
27. R. K. Wang, L. An, P. Francis, and D. J. Wilson, "Depth-resolved imaging of capillary networks in retina and choroid using ultrahigh sensitive optical microangiography," Opt. Lett. **35**(9), 1467–1469 (2010).
28. L. An and R. K. Wang, "In vivo volumetric imaging of vascular perfusion within human retina and choroids with optical micro-angiography," Opt. Express **16**(15), 11438–11452 (2008).
29. S. Makita, F. Jaillon, M. Yamanari, M. Miura, and Y. Yasuno, "Comprehensive in vivo micro-vascular imaging of the human eye by dual-beam-scan Doppler optical coherence angiography," Opt. Express **19**(2), 1271–1283 (2011).
30. F. Jaillon, S. Makita, E.-J. Min, B. H. Lee, and Y. Yasuno, "Enhanced imaging of choroidal vasculature by high-penetration and dual-velocity optical coherence angiography," Biomed. Opt. Express **2**(5), 1147–1158 (2011).
31. S. Zotter, M. Pircher, T. Torzicky, M. Bonesi, E. Götzinger, R. A. Leitgeb, and C. K. Hitzenberger, "Visualization of microvasculature by dual-beam phase-resolved Doppler optical coherence tomography," Opt. Express **19**(2), 1217–1227 (2011).
32. G. Liu, W. Qi, L. Yu, and Z. Chen, "Real-time bulk-motion-correction free Doppler variance optical coherence tomography for choroidal capillary vasculature imaging," Opt. Express **19**(4), 3657–3666 (2011).
33. P. Meemon and J. P. Rolland, "Swept-source based, single-shot, multi-detectable velocity range Doppler optical coherence tomography," Biomed. Opt. Express **1**(3), 955–966 (2010).
34. I. Grulkowski, I. Gorczynska, M. Szkulmowski, D. Szlag, A. Szkulmowska, R. A. Leitgeb, A. Kowalczyk, and M. Wojtkowski, "Scanning protocols dedicated to smart velocity ranging in spectral OCT," Opt. Express **17**(26), 23736–23754 (2009).
35. J. Barton and S. Stromski, "Flow measurement without phase information in optical coherence tomography images," Opt. Express **13**(14), 5234–5239 (2005).
36. A. Mariampillai, B. A. Standish, E. H. Moriyama, M. Khurana, N. R. Munce, M. K. K. Leung, J. Jiang, A. Cable, B. C. Wilson, I. A. Vitkin, and V. X. D. Yang, "Speckle variance detection of microvasculature using swept-source optical coherence tomography," Opt. Lett. **33**(13), 1530–1532 (2008).
37. J. Enfield, E. Jonathan, and M. Leahy, "In vivo imaging of the microcirculation of the volar forearm using correlation mapping optical coherence tomography (cmOCT)," Biomed. Opt. Express **2**(5), 1184–1193 (2011).
38. B. H. Park, M. C. Pierce, B. Cense, S.-H. Yun, M. Mujat, G. J. Tearney, B. E. Bouma, and J. F. de Boer, "Real-time fiber-based multi-functional spectral-domain optical coherence tomography at 1.3 µm," Opt. Express **13**(11), 3931–3944 (2005).

#157238 - $15.00 USD Received 28 Oct 2011; revised 9 Dec 2011; accepted 11 Dec 2011; published 21 Dec 2011

39. S. Makita, F. Jaillon, M. Yamanari, and Y. Yasuno, Computational Optics Group, University of Tsukuba, 1–1-1 Tennodai, Tsukuba, Ibaraki 305–8573, Japan, are preparing a manuscript to be called "Dual-beam-scan Doppler optical coherence angiography for birefringence-artifact-free vasculature imaging."
40. P. Amalric, "The choriocapillaris in the macular area," Int. Ophthalmol. **6**(2), 149–153 (1983).
41. S. S. Hayreh, "Physiological anatomy of the choroidal vascular bed," Int. Ophthalmol. **6**(2), 85–93 (1983).
42. J. J. De Laey, "Fluorescein angiography of the choroid in health and disease," Int. Ophthalmol. **6**(2), 125–138 (1983).
43. C. Wang, Z. Ding, M. Geiser, T. Wu, and M. Chen, "Choroidal laser Doppler flowmeter with enhanced sensitivity based on a scattering plate," J. Biomed. Opt. **16**(4), 047004 (2011).

1. Introduction

Increased knowledge of the choroidal vasculature is important for developing our understanding of retinal pathologies, such as age-related macular degeneration (AMD), in which decreased choroidal perfusion occurs, leading to the onset of neovascularization (CNV) [1–5]. Regular screening of the choroidal vasculature enables early detection of abnormalities, and this is essential when considering effective treatment regimens. Thus, imaging techniques that enable early detection of emerging abnormal vessels are of great importance. A standard technique for imaging the vasculature is indocyanine green angiography (ICGA). However, ICGA requires dye injections and can have adverse effects. Therefore, the use of non-invasive techniques for the analysis of choroidal circulation is preferable. This led us to employ optical coherence tomography (OCT) as a means for such analyses.

Over the past two decades, OCT [6] has proven its clinical value for imaging the eye and for providing two-dimensional (2-D) and three-dimensional (3-D) non-invasive *in vivo* biopsies of anterior eye segments [7,8] and the retina [9–12]. Moreover, one-micrometer wavelength systems have demonstrated an enhanced ability to penetrate deeper into the choroid when compared to 800 nm systems [13–17]. In addition to structural information provided by the backscattered intensity of OCT signals, this technique also gives access to flow information through Doppler phase shifts of the complex OCT signal. The latter allows assessment of blood velocity, or flow, inside vessels. The phase-resolved method [18,19], using the phase difference between adjacent A-lines, simultaneously accomplishes high-speed imaging and high-velocity sensitivity. In this paper, we refer to this technique as "conventional Doppler OCT". Subsequently, during the past decade, improvements in conventional Doppler OCT and new approaches have been proposed for visualizing flows: phase-based [20–34] and intensity-based [35–37]. In particular, among these studies, the aim was to further improve the Doppler OCT technique in order to more comprehensively visualize the choroidal vasculature.

Our group has previously used dual-beam optical coherence angiography (DB-OCA), and we have demonstrated the enhanced flow sensitivity of this approach when imaging retinal and choroidal vessels, without decreasing acquisition time [29,30]. However, one limitation of the DB-OCA system is that the separation between the two beams is fixed, which is a drawback when wishing to modify the measurable velocity range of blood flow. In order to increase or decrease the time delay (T) between beams, it is necessary to increase or decrease the number of A-lines between the beams. This modifies the spatial sampling (i.e., the distance between A-lines), and can lead to the degradation of image quality. We therefore propose a more flexible DB-OCA system with variable beam separation that provides variable Doppler flow ranges. Here, we present the new system for choroidal vasculature imaging in human eyes.

2. Methods

2.1 Dual-beam method

The protocol for the dual-beam method can be found elsewhere [29,30]. Briefly, in the DB-OCA method, two beams scan the sample with the same scanning speed (v_s) but with a

#157238 - $15.00 USD Received 28 Oct 2011; revised 9 Dec 2011; accepted 11 Dec 2011; published 21 Dec 2011

spatial separation (*d*). With respect to the preceding beam (B_1), the following beam (B_2) probes the same lateral location after a delay of $T = d / v_s$. Therefore, by denoting the axial depth by z and the time by t, acquired signals $S_1(z, t)$ and $S_2(z, t + T)$ of B_1 and B_2, respectively, correspond to the same lateral position. The phase difference $\Delta\phi(z,t)$ between the two signals at a given depth can then be computed as $\Delta\phi(z,t) = \phi_1(z,t) - \phi_2(z,t+T)$, where ϕ_1 and ϕ_2 are phases of B_1 and B_2, respectively. The axial velocity (v_z) of the existing flow at this location is calculated as:

$$v_z = \frac{\lambda_0 \Delta\phi}{4\pi\, nT}, \tag{1}$$

where λ_0 is the source wavelength, and n is the refractive index of the tissue. Using the phase-resolved method and since $-\pi < \Delta\phi < \pi$, the range of detectable velocities is given by [38]:

$$\frac{\lambda_0}{4\pi n\, T}\ \sqrt{\frac{1}{SNR}} \le \left|v_z\right| \le \frac{\lambda_0}{4nT}, \tag{2}$$

where *SNR* is the signal-to-noise ratio. The delay $T = p\ .\ t_A$, where t_A is the time interval between A-lines and where p is an integer ≥1. Therefore, the DB-OCA method can probe flows with slower velocities compared to conventional phase-resolved Doppler OCT (phase difference between adjacent A-lines), whose velocity range is given by:

$$\frac{\lambda_0}{4\pi n\, t_A}\ \sqrt{\frac{1}{SNR} + \sigma_{\Delta x}^2} \le \left|v_z\right| \le \frac{\lambda_0}{4nt_A}, \tag{3}$$

where $\sigma_{\Delta x}$ is the phase noise arising from spatial decorrelation between adjacent A-lines. $\sigma_{\Delta x}$ indicates that in conventional Doppler OCT, flow sensitivity is degraded by spatial decorrelation between A-lines, while DB-OCA is free from this negative effect as long as motions are small enough to be numerically compensated. Note that DB-OCA can also provide conventional Doppler signals if we apply a dense A-line scanning protocol. Indeed, in this study, as in a previous study [30], we separately computed the conventional Doppler OCT for both beams of DB-OCA and averaged them to provide a conventional Doppler OCT image, in addition to the DB-OCA images. Also, in OCA procedure [23], compensation algorithms are used to compensate axial bulk motion in each A-line and motions between frames (B-scan).

In our previously published DB-OCA study [29,30], beam separation was fixed and, as described in the introduction, comparisons between vasculature images acquired with fixed beam separation and different scanning steps is difficult. Therefore, in the next section, we propose a technical solution for adjusting beam separation without changing the scanning protocol.

2.2 Dual-beam optical coherence angiography with variable beam separation

DB-OCA utilizes polarization multiplexing to generate two beams. Therefore, it is important to note that our sample, reference, and detection arms are composed of polarization maintaining fibers. As described in the previous section, if the time separation, *T,* between the two scanning beams is variable, it allows the measurable velocity range [Eq. (2)] of blood flow to be changed. Therefore, in order to enable variable beam separation, we have implemented a technical solution in the scanning head. The schematic of the scanning head is

#157238 - $15.00 USD Received 28 Oct 2011; revised 9 Dec 2011; accepted 11 Dec 2011; published 21 Dec 2011

shown in Fig. 1. The two beams are generated by means of a polarization beam splitter (PBS) (5 mm × 5 mm × 5 mm; Thorlabs, NJ) and three gold mirrors (5 mm × 7 mm).

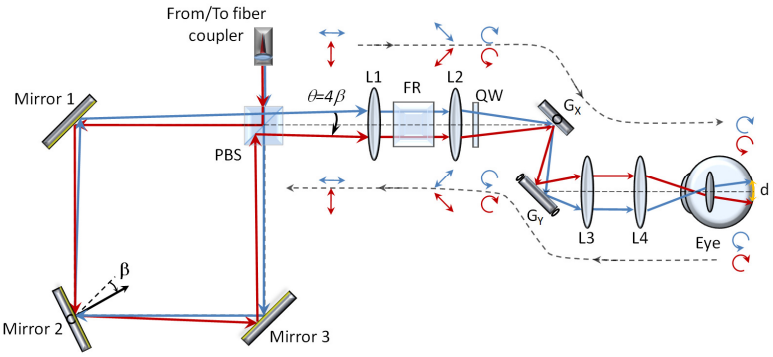

Fig. 1. Schematic of the scanning head for dual-beam OCA with variable-beam separation. By rotating Mirror 2, the beam separation d can be varied. Mirrors 1 and 3 are fixed. Faraday rotator (FR), Quarter wave plate (QW), galvano-scanners (Gx, Gy). Red and blue arrows represent the polarization states from the PBS to the eye in the plane perpendicular to propagation (backward and forward directions).

The distance between the mirrors and the PBS is approximately 20 mm. Light incoming from the fiber coupler is split into two beams characterized by their states of polarization, i.e., parallel (to the figure plane, blue) and perpendicular (to the figure plane, red). The surfaces of Mirror 1 and Mirror 3 are fixed such that their normal directions are at an angle of 45 degrees with respect to the direction of the incident light emerging from the PBS. Both states of polarization are then reflected and are directed to Mirror 2. If the surface of Mirror 2 is at an angle of 45 degrees ($\beta = 0$) to the incoming light, then the two states of polarization have the same direction after the PBS and no angular or spatial separation exists on the retina. Mirror 2 is not fixed and can be rotated around an axis that is perpendicular to the plane of Fig. 1. By rotating this mirror with an angle β, the two states of polarization are spatially separated and have an angular separation at the exit of the PBS, equal to 4β. Note that Mirror 2 is positioned at the conjugate of the eye pupil. Achromatic lenses L_1 and L_2 are used (focal lengths: f_1 = 75 mm and f_2 = 150 mm) to relay the two beams through the Faraday rotator. The utilization of a Faraday rotator and quarter wave plate is designed to suppress birefringence artifacts [39]. After reflection on galvano scanners (x- and y-directions), light successively passes through an achromatic lens (L_3, f_3 = 60 mm) and an ophthalmic lens L_4 (40D; Volk, Mentor, OH). Finally, due to the rotation of Mirror 2, the two beams reach the retina with a spatial separation, d. We can therefore adjust the rotation angle, β, to have the desired beam separation, d, on the retina. Light is then backscattered and is redirected to the detection arm. The evolution of polarization states in the plane perpendicular to propagation are indicated in Fig. 1 (red and blue arrows).

3. Setup

The scanning head described in the previous section is integrated into the DB-OCA system depicted in Fig. 2. A broadband SLD light source (Superlum, Ireland) at 1020 nm with a bandwidth (full-width-half-maximum; FWHM) of 100 nm is used. The axial resolution has been measured as 5.3 μm in tissue. An isolator is placed after the light source to hinder back reflections. After the isolator, a polarization controller is used to balance both states of polarization reflected from the reference arm. Then, light is directed through polarization maintaining fibers into a 2 × 2 optical coupler (50:50 split ratio; General Photonics, CA), where the light is split into the sample and reference arms. Note that polarization-maintaining

#157238 - $15.00 USD Received 28 Oct 2011; revised 9 Dec 2011; accepted 11 Dec 2011; published 21 Dec 2011

fibers are used in the interferometer and spectrometer (green lines). The sample arm is attached to the scanning head shown in Fig. 1, and is described in the previous section. The incident power on the cornea is 1.68 mW in total of two polarization states. The beam diameter on the retina is estimated to be 14 μm (FWHM) according to a ray-tracing simulation. Backscattered light from the retina is propagated back to the interferometer where it interferes with the reference light. It is then directed to a fiber-based PBS that separates and redirects the two polarization states to two identical spectrometers. In both spectrometers, a blazed diffraction grating is used (1200 lp/mm, Thorlabs, NJ) and InGaAs line-scan cameras (46,900 lines/s, SUI1024LDH-1.7 RT-0500LC; Sensors Unlimited Inc., Goodrich, NJ) collect interference spectra. The measured sensitivities of each detection channel, which correspond to each spectrometer and each polarization state, are 91.3 (blue beam in Fig. 1) and 93.6 dB (red beam in Fig. 1). A possible explanation for the different sensitivities would be the polarization dependency of the PM coupler and that of the PBS in the scanning head. Moreover, collection efficiency of backscattered light between the two beams may be different. Synchronization of data acquisition and galvano scanners is achieved by control signals from a function generator board (PCI-6713, National Instruments, TX) connected to a standard PC.

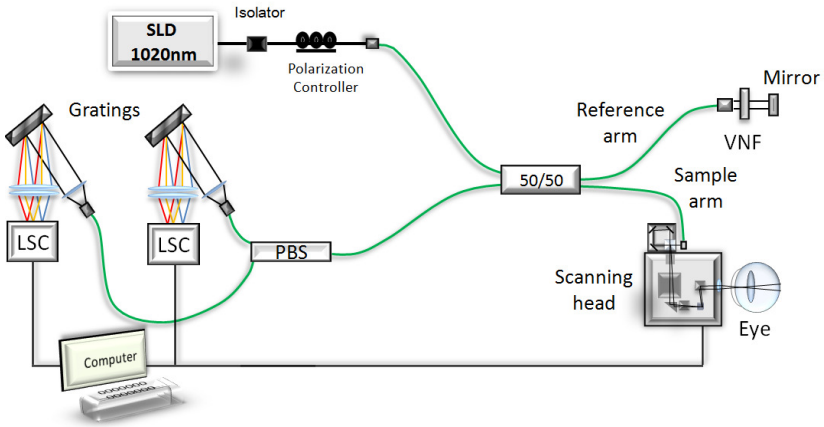

Fig. 2. Schematic of the double beam SD-OCT setup. Variable neutral filter (VNF). Line scan camera (LSC). Green lines represent polarization-maintaining (PM) fibers, Polarization Beam Splitter (PBS).

The lateral distance between the two beams is determined by measuring a static scattering sample. A homogenous area of the sample is chosen and two B-scans, simultaneously obtained from the two beams, are considered. The lateral direction of one B-scan with respect to the other is then numerically shifted. The phase difference squared is computed as a function of the lateral shift. When the phase difference squared reaches a minimum, it means that each A-line of the B-scan corresponding to the preceding beam is superimposed with its counterpart of the B-scan of following beam. Moreover, tiny adjustments (+/–0.1% of the scanning range) of galvanometer voltage can also be carried out in order to correct for sub-pixel shifts between B-scans.

4. Results and discussion

4.1 Choroidal velocity maps

Using the one-micron wavelength DB-OCA setup described in previous sections, 3-D volumes of the choroidal vasculature from a normal emmetropic eye (right eye, 35-yr-old man) were acquired, for five different beam separations. Each volume consisted of 1000 A-lines (horizontal, x-direction) × 256 B-scans (vertical, y-direction) × 1024 depths (z-

#157238 - $15.00 USD Received 28 Oct 2011; revised 9 Dec 2011; accepted 11 Dec 2011; published 21 Dec 2011

direction) voxels. The acquisition time for each volume was approximately 6 s. The scanned area (x-y) was 4 mm × 4 mm. Volumes were acquired for five beam separations: T = 0.220, 0.396, 0.726, 1.254, and 1.628 ms. Conventional Doppler OCT was available in all acquired volumes, as explained in section 2.1. For each beam separation, nine different locations were acquired from the macula to the optic nerve head (ONH) by changing the position of a fixation target. The location of retinal pigment epithelium (RPE) was used to separate the choroid from the retina in each B-scan (see Fig. 3(a)). From this estimated RPE border, the average of absolute axial velocity $|v_z|$ (from Eq. (1)) was computed over a depth of 264 μm (from 10 pixels to 90 pixels below RPE). This provides 2D (x-y) choroidal $|v_z|$ maps (1000 × 256). Note here that it is difficult to exclude static tissue when the average is carried along the depth (Fig. 3(b)). Therefore, our average over depth contains vessels and static tissue which implies underestimation of the real axial velocity inside the vessel.

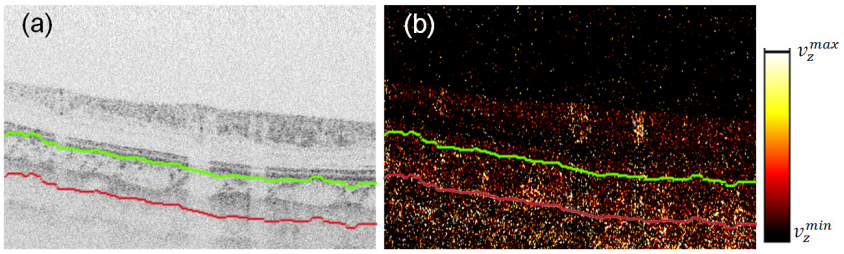

Fig. 3. B-scans displaying the intensity (a) and axial velocity (b) of posterior eye. Choroid region is defined by upper (green line) and lower (red line) limits.

Three examples are shown in Fig. 4. The location shown is inferior to the ONH. Figure 4(a) corresponds to conventional Doppler OCT (t_A = 0.022 ms), Fig. 4(b) to DB-OCA with a time delay of T = 0.396 ms, and Fig. 4(c) to T = 1.628 ms. Note that Fig. 4(c) was acquired at a location that was a little different to that of Figs. 4(a) and 4(b). This is because Figs. 4(a) and 4(b) were acquired simultaneously, whereas Fig. 4(c) was acquired at a different session. Indeed, as mentioned in section 2.1, conventional Doppler can be computed from the same volumetric data of DB-OCA as shown in Figs. 4(a) and 4(b), where Fig. 4(a) is conventional Doppler and Fig. 4(b) is DB-OCA with T = 0.396 ms. Then, we manually change the beam separation and acquire another DB-OCA with T = 1.628 ms (Fig. 4(c)). From these three examples, different choroidal vasculatures can clearly be observed. Note that retinal vessels that are visible in choroidal velocity maps are due to decorrelation shadows. As can be seen in these 2-D velocity maps, image contrast is not optimal since we displayed all velocities corresponding to a phase shift ranging from 0 to π. Therefore, optimization of the display range is discussed in the next section.

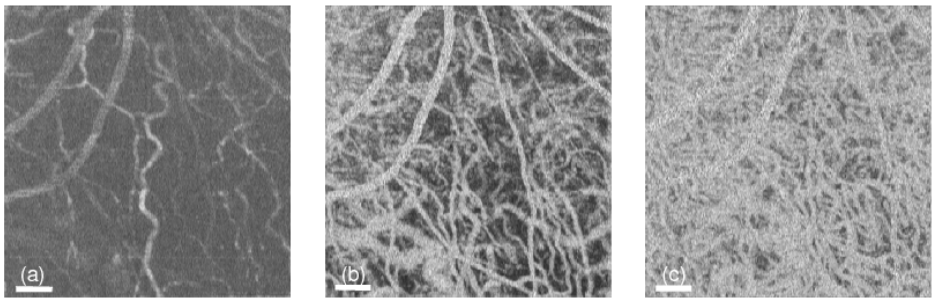

Fig. 4. En-face projection (average) of absolute axial velocity ($|v_z|$) for choroidal vasculature: (a) with conventional Doppler: t_A = 0.022 ms and (b) with Dual Beam: T = 0.396 ms, (c) T = 1.628 ms. The scale bar represents 500 μm.

#157238 - $15.00 USD Received 28 Oct 2011; revised 9 Dec 2011; accepted 11 Dec 2011; published 21 Dec 2011

4.2 Optimization of signal range for display

In order to enhance the contrast of en-face choroidal velocity maps, optimization of the signal range for display was performed. This optimization was carried out by selecting a proper minimum display range as follows. For each beam separation, we computed the velocity distribution of the 2-D map. In Fig. 5, the Doppler signal distributions are shown for each beam separation as histograms. Normalization by the sum of counts over all velocities has been carried out. Figure 5(a) explicitly displays the velocity distribution in the case of the conventional Doppler. A zoomed area of Fig. 5(a) is shown in Fig. 5(b) and corresponds to velocity distributions acquired with DB-OCA, where T is the delay between two beams. From the velocity distribution, we then selected a threshold value. This threshold value was chosen to be the velocity corresponding to the maximum count of velocity distribution, computed from en-face velocity maps. We assumed that this maximum corresponds to noise background and applied a mask that sets velocities lower than the chosen threshold value to 0. This threshold procedure is intended to enhance image contrast or optimize display range of major vessels. It is not designed to remove noise. Therefore, signal of low-flow vessels may be lost. The displayed velocities are those indicated by the light blue regions in Fig. 5. Applying this mask and a blurring filter with a 3 × 3-pixel Gaussian kernel to the examples given in Fig. 4 yields the en-face maps shown in Fig. 6. In the following section, we used these velocity maps with this optimal range to build a wide-field fundus mosaic. This provided an extended view of the choroidal vasculature from the ONH to the macula. Note that in the case of the mosaic, we included all en-face velocity maps (corresponding to different locations on the retina) to generate the velocity distribution and obtain the threshold value.

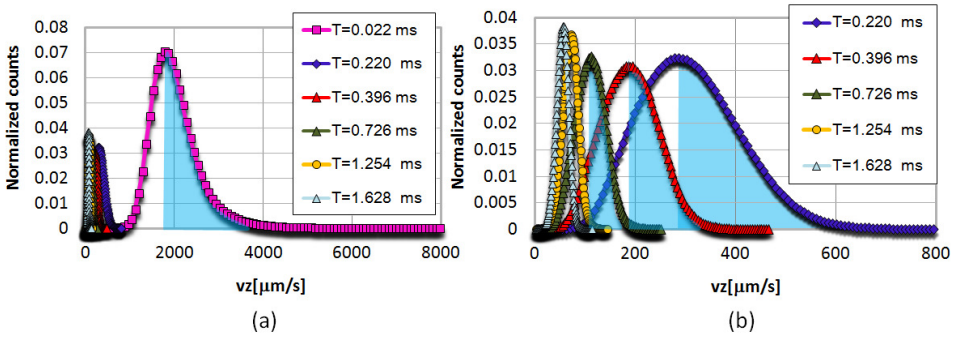

Fig. 5. Experimental velocity distributions of en-face velocity maps for different beam separations. (a) all delays (b) zoomed area of (a) on small velocities.

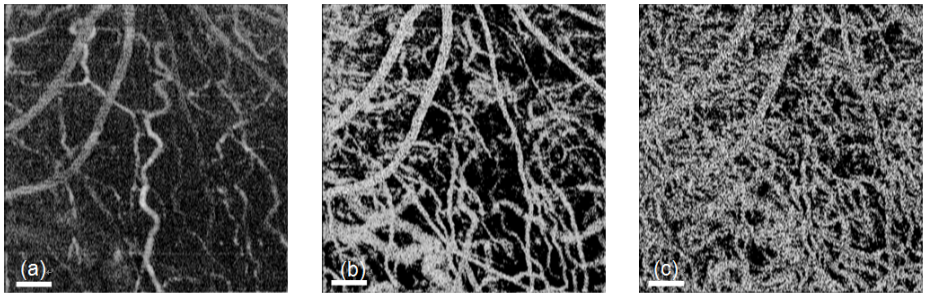

Fig. 6. En-face projection (average) with applied threshold of absolute axial velocity ($|v_z|$) for choroidal vasculature: (a) with conventional Doppler: t_A = 0.022 ms, and (b) with Dual Beam: T = 0.396 ms, (c) T = 1.628 ms. The scale bar represents 500 µm.

#157238 - $15.00 USD Received 28 Oct 2011; revised 9 Dec 2011; accepted 11 Dec 2011; published 21 Dec 2011

4.3 Choroidal vasculature mosaics

After the optimization of the signal range was achieved as described in the previous section, we manually stitched the en-face velocity maps together and generated a mosaic of the choroidal vasculature for each different beam separation as shown in Fig. 7. The mosaic covered an area of approximately 9 × 9 mm^2, from the ONH to the macula (the fovea is indicated by white circles). Each mosaic is made of 9 en-face velocity maps. Therefore one session takes approximately three minutes. Figure 7(a) shows choroidal vasculatures obtained with conventional Doppler OCT with t_A = 0.022 ms. Figures 7(b)–7(f) show choroidal vasculatures obtained with 5 beam separations: T = 0.220 ms (Fig. 7(b)), T = 0.396 ms (Fig. 7(c)), T = 0.726 ms (Fig. 7(d)), T = 1.254 ms (Fig. 7(e)), T = 1.628 ms (Fig. 7(f)). Velocity ranges, shown below each mosaic, correspond to absolute axial velocity $|v_z|$ computed from Eq. (1). It should be mentioned that these velocities are axial velocities and are therefore dependent on the angle of the incident light.

Figure 7(a) corresponds to the conventional Doppler OCT, and is therefore more sensitive to high-flow vessels, such as arteries. Vessels with relatively high signals observed in the peripapillary region (Fig. 7(a), blue arrows) are clearly short posterior ciliary arteries. Moreover, in the foveal region, no large arteries are visible, confirming previous results obtained with fluorescein angiography [40]. Only short arteries are seen in the perimacular region (yellow circles in Fig. 7(a)). The latter usually reach the choriocapillaris in a perpendicular and abrupt manner [41]. It is important to note here, that except for some choroidal arteries whose direction is mainly axial, most of the choroidal vasculature lies in a plane that is nearly perpendicular to the incident light. Therefore, the actual velocity is much higher than the axial velocity shown by the corresponding color map.

With this system, we can change the time delay, T, between the two beams without modifying the scanning protocol. This is shown in Figs. 7(b)–7(f), where five delays of T have been tested from 0.22 to 1.628 ms. As previously mentioned, we have access to the axial velocity $|v_z|$ and the incident light is almost perpendicular to the vessel direction. Therefore, the Doppler shift is small. In some cases, a change of contrast between adjacent maps is visible (see regions located on the right and left side of the dashed red line in Fig. 7(c)). These changes are due to a different incident angle of probing light with respect to the choroid between adjacent maps (acquired in different sessions). The increase in T enables the visualization of choroidal vessels that are undetected by conventional Doppler, and from these mosaics we clearly verify that as T gets larger, the sensitivity increases and denser choroidal vasculature appears. We also observe that high-flow vessels are still visible. Indeed, due to phase ambiguity and phase wrapping, this technique does not act as a velocity band-pass filter. Doppler signals of high-flow vessels, while strongly reduced, are not totally suppressed. One way to deal with this issue, for example, would be to generate velocity maps from the subtraction between signals acquired with a different beam separation. Another observation is that for all time delays, the contrast of choroidal vessels is higher in the periphery than in the macular region. One explanation for lower contrast is that the macular region has the densest choroidal venous network [42]. A second explanation is that choroidal thickness is larger in the macular region than in the peripheral regions. Therefore, choroid vessels are not entirely probed and the averaged Doppler signal along the depth is less contrasted. It should be pointed out here that the probed eye was emmetropic, which means that choroid thickness is greater than that of myopic eyes. Thus, better contrast is expected in the case of myopic eyes.

Wang et al. have published measurements with laser Doppler flowmetry showing an approximate red blood cell axial velocity of 0.4~1 mm/s in the human choroidal vascular bed (apart from arteries) [43]. This is comparable to our results. Combining velocity maps with different beams separations can provide more information about choroidal circulation and location; this is done in the next section.

#157238 - $15.00 USD Received 28 Oct 2011; revised 9 Dec 2011; accepted 11 Dec 2011; published 21 Dec 2011

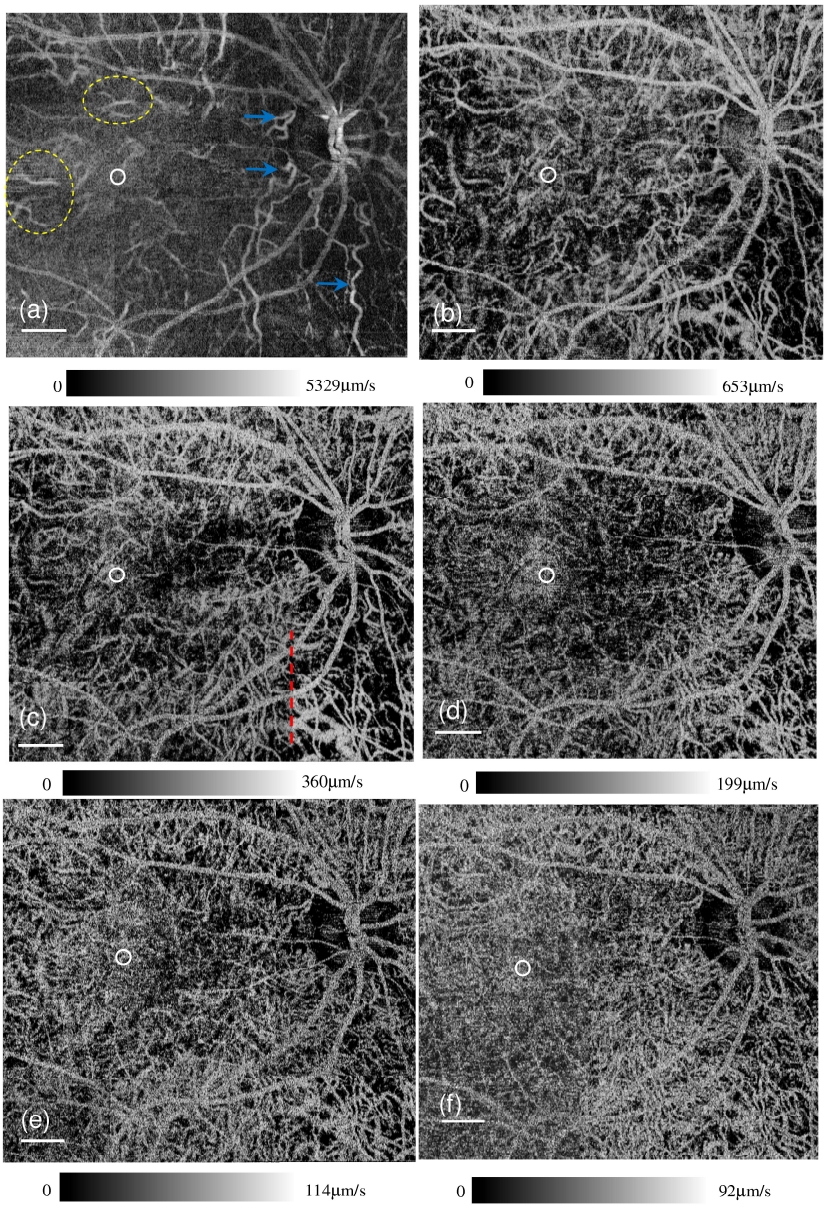

Fig. 7. En-face projection mosaics of choroidal vasculature (axial velocity) for different beam separations: (a) t_A = 0.022 ms, (b) T = 0.220 ms, (c) T = 0.396 ms, (d) T = 0.726 ms, (e) T = 1.254 ms, (f) T = 1.628 ms. The scale bar represents 1 mm. White circles show the position of the fovea. See details in text.

4.4 Composite mosaic of choroidal vasculature

The choroidal vasculature displayed in Fig. 7(f) was acquired with a delay of T = 1.628 ms. While more vessels are visible compared to images obtained with smaller time delays, low-flow and high-flow vessels are not distinguishable. Therefore, a better representation can be achieved by generating a composite mosaic, which associates a color to each mosaic according to its beam delay. This is shown in Fig. 8 where we have superimposed velocity mosaics V_{T1}(x, y), V_{T2}(x, y), V_{T3}(x, y), and V_{T4}(x, y) acquired with delays T_1 = 0.022 ms (color

#157238 - $15.00 USD Received 28 Oct 2011; revised 9 Dec 2011; accepted 11 Dec 2011; published 21 Dec 2011

C_{T1}: pink), T_2 = 0.220 ms (C_{T2}: blue), T_3 = 0.396 ms (C_{T3}: red), and T_4 = 1.254 ms (C_{T4}: orange), respectively. We manually modified the display range to enhance visibility, as indicated in the legend where axial velocity ranges are given. We gave priority to lower time delays. In other words, for a given pixel (x, y), its color C is given by:

$$C = \begin{cases} C_{T1} \ \ if\ V_{T1} \neq 0 \\ \quad else \begin{cases} C_{T2} \ \ if\ V_{T2} \neq 0 \\ \quad else \begin{cases} C_{T3} \ \ if \ \ V_{T3} \neq 0 \\ \quad else \ \ V_{T4} \end{cases} \end{cases} \end{cases} . \tag{4}$$

We additionally overlaid the retinal vessels (white) obtained using the DB-OCA method (delay T_3 = 0.396 ms). In this composite mosaic, we positioned images acquired with lower delays on top. By doing so, the possibility that visible low-velocity vessels (long delay T), originating from phase wrapping, might obscure high-velocity vessels is reduced.

The combination of choroidal vasculature images acquired with different beam separations allows us to clearly distinguish vessels with respect to their blood flow axial velocity. The composite image of the choroidal circulation therefore provides the ability of spatially discriminating vessels according to the axial velocity range of their blood content. In the ONH region and excluding central retinal arteries and veins, it is difficult to determine the layer to which visible structures belong. Indeed, RPE segmentation is impossible in this area. Again, we provided axial velocity ranges in Fig. 8, but these ranges are strongly dependent on the incident angle, θ, of light with respect to vessel direction. This angle is clearly close to 90 degrees, and consequently absolute blood velocities are much higher than the axial velocities shown. Currently, the two main limitations of our system are the acquisition time of the detectors (47 kHz) and the manual change of the beam separation. Dual beam method

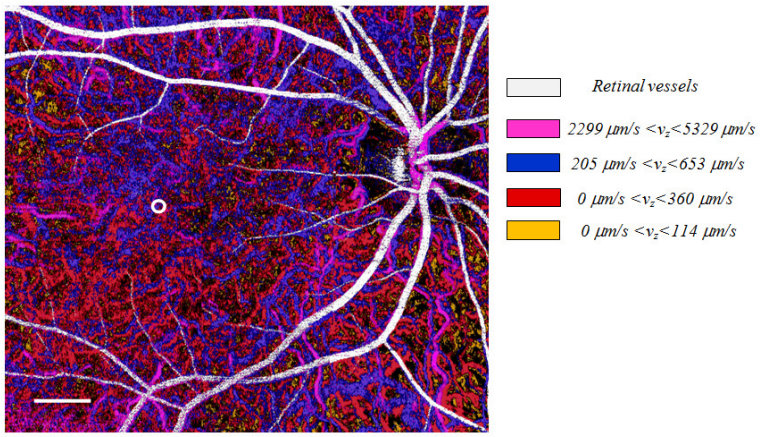

Fig. 8. Composite mosaic of choroidal vasculature with different colors corresponding to different delays: T = 0.022 ms (pink), 0.220 ms (blue), 0.396 ms (red), and 1.254 ms (orange). Retinal vessels are shown in white. The white circle shows the position of the fovea. The scale bar represents 1 mm.

can be applied with faster detectors that are already commercially available. Moreover, the mirror rotation that allows altering the beam separation can be motorized. This will enable rapid beam separation selection and thus solves registration issues between volumes acquired using different beam separation. Consequently, applying these modifications will enable the system to acquire multi-beam separation volumes within acceptable durations for clinical purposes.

#157238 - $15.00 USD Received 28 Oct 2011; revised 9 Dec 2011; accepted 11 Dec 2011; published 21 Dec 2011

5. Conclusion

We have proposed a technical modification to one-micrometer wavelength DB-OCA to enable variable beam separation. This allows selectable velocity ranges of detectable Doppler signals, without changing scanning protocols. Choroidal vasculatures were imaged using different beam delays ranging from 0.22 to 1.628 ms. This system represents a trade-off between the number of vessels that can be visualized and their contrast. This study also demonstrates the advantage of combining 2-D velocity maps, acquired with different beam separations, to provide a more complete representation of the choroidal circulation. We hope that this method will improve assessment and screening of choroidal vasculature abnormalities that exist in pathological conditions of the eye.

Acknowledgments

This study was partially supported by the Japanese Science and Technology Agency through a contract for the Development of Systems and Technology for Advanced Measurement and Analysis.

#157238 - $15.00 USD Received 28 Oct 2011; revised 9 Dec 2011; accepted 11 Dec 2011; published 21 Dec 2011